Journal of Computational and Applied Mechanics, Vol. 17, No. 2, (2022), pp. 105–123
DOI: 10.32973/jcam.2022.006

INVESTIGATION OF MICRO-SHOCK WAVES IN A PLANAR MAGNETOGASDYNAMIC FLOW USING THE DISCONTINUOUS GALERKIN FINITE ELEMENT METHOD

Alberto Gallottini
Centre for Computational Engineering Sciences, Cranfield University, Cranfield, Bedfordshire, MK43 0AL, United Kingdom
alberto.gallottini@cranfield.ac.uk

László Könözsy
Centre for Computational Engineering Sciences, Cranfield University, Cranfield, Bedfordshire, MK43 0AL, United Kingdom
laszlo.konozsy@cranfield.ac.uk

[Received: October 24, 2022; Accepted: December 21, 2022]

Abstract. The present work focuses on the numerical investigation of micro-shock wave propagation in a two-dimensional magnetogasdynamic flow in the framework of the Discontinuous Galerkin-Finite Element Method (DG-FEM). The Lorentz force has been implemented in the compressible, viscous Navier–Stokes equations as a source term using first-order spatial and fourth-order temporal Runge–Kutta discretization schemes. To investigate the effect of the electrical conductivity on the micro-shock wave propagation, a two-dimensional micro-shock channel problem with hydraulic diameter of 2.5 mm, length of 82 mm, and no-slip boundary conditions at the left and at the right wall is considered as a benchmark problem. In this case, acoustic waves are generated behind after the rupture of the membrane that separates two states of the same gas originally at different pressure and density and both initially at rest. The magnetic field is taken into account as uniform and stationary throughout the microchannel, and the numerical simulations are performed in a short physical time, before the reflection of the waves on the lateral wall. A detailed parametric study of the temperature, density, pressure, and u-velocity is carried out by a variation of the electrical conductivity of the magnetogasdynamic flow, under the assumption of low magnetic Reynolds numbers. It has been found that the jumps of the acoustic waves become significantly intensified when the electrical conductivity of the gas is increased. It has also been observed that the presence of the Lorentz force causes an acceleration in the gasflow towards the outlet section of the microchannel at the low Knudsen number of 0.05. The outcome of this research work could be relevant to biomedical applications where the ability to control the flow in a microchannel has a significant impact on the development of small devices aimed to deliver pharmaceutical drugs in specific locations.

Mathematical Subject Classification: 76N30, 76M10, 76M12, 76W05
Keywords: Magnetogasdynamics, microfluidics, discontinuous Galerkin (DG) method

Nomenclature

Acronyms

DG-FEM	Discontinuous Galerkin-Finite Element Method
EHD	Electrohydrodynamics
FDM	Finite Difference Method
FEM	Finite Element Method
FVM	Finite Volume Method
IVP	Initial Value Problem
LSERK	Low Storage Explicit Runge–Kutta
MGD	Magnetogasdynamics
MHD	Magnetohydrodynamics
ODE	Ordinary Differential Equation
PDE	Partial Differential Equation

Greek Symbols

γ	Specific heat capacity	[–]
μ	Dynamic viscosity	$[\mathrm{Pa}\cdot\mathrm{s}]$
μ_0	Magnetic permeability	[H/m]
Ω	Physical domain	$[\mathrm{m}^2]$
Ω_h	Computational domain	$[\mathrm{m}^2]$
ϕ_h	Test function	[–]
ρ	Fluid density	$[\mathrm{kg/m}^3]$
σ	Electrical conductivity	[S/m]
$\underline{\underline{\tau}}$	Viscous stress tensor	[Pa]
$\underline{\underline{S}}$	Rate-of-strain tensor	[1/s]

Roman Symbols

$\bar{v}$	Mean velocity along the height of the microchannel	[m/s]
ℓ	Characteristic length	[m]
$\hat{\mathbf{n}}$	Normal unit vector	[–]
$\mathbf{B}$	Magnetic flux density	[T]
$\mathbf{f}$	Flux vector	
$\mathbf{f}^*$	Numerical flux vector	
$\mathbf{f}_h$	Approximated flux vector	
$\mathbf{F}_L$	Lorentz force	[N]
$\mathbf{j}$	Electric current density	$[\mathrm{A/m}^2]$
$\mathbf{u}$	Conservative variables vector	
$\mathbf{u}_h$	Approximated conservative variables vector	
$\mathbf{v}$	Velocity field of the fluid flow	[m/s]
$\underline{\underline{I}}$	Unit tensor	[–]
D_k	k-th triangular element	$[\mathrm{m}^2]$
E	Total energy per unit volume	$[\mathrm{J/m}^3]$
F_{L_x}	x-component of the Lorentz force in Cartesian coordinates	[N]
F_{L_y}	y-component of the Lorentz force in Cartesian coordinates	[N]
H_y	y-component of the magnetic field intensity	[T]
k	Thermal conductivity coefficient	$[\mathrm{W}/(\mathrm{m}\cdot\mathrm{K})]$
l_i^k	Multidimensional Lagrange polynomial	[–]
Re_m	Magnetic Reynolds number	[–]
u, v	Velocity components in Cartesian coordinates	[m/s]

1. Introduction

Magnetohydrodynamics (MHD), [1, 2] including magnetogasdynamics (MGD), has attracted the attention of researchers in the last decade in relation to the growing field of microfluidics applications. The reason is that it is possible to replicate many of the traditional analyses in a single chip made in a chemical laboratory through the integration of several components (e.g., microchannel, micropumps, mixers and microvalves). Among all the different industries, lab on a chip devices are particularly used in the biomedical area as drug delivery systems or for manipulation of cells and detection of small analytes. These portable and low-cost devices are used, for instance, to detect and isolate the rare circulating tumour cells (CTCs) detached from a primary tumour [3] or to perform a DNA sequencing analysis [4]. Magnetic drug targeting is a promising treatment to avoid the collateral effect of a cancer drug by adopting magnetic nanocarriers which are tied to the drug and then delivered to the specific tissue through the application of an external magnetic field [5]. Therefore, in this work, a magnetogasdynamic microflow benchmark problem is investigated to understand better the physics of micro-shock wave propagation in the presence of a uniform and stationary magnetic field, which could be relevant to biomedical applications. It could be important in applications where the ability to control the gasflow in a microchannel has an impact on the development of microfluidic devices aimed to deliver pharmaceutical drugs in specific locations.

In comparison with macroscopic fluid dynamics, shrinking the length of a device can change the physical and chemical behavior of fluids quite intensively, allowing interesting phenomena such as electrokinetics, magnetohydrodynamics, and capillarity effects that are not necessarily present in macro-scale fluid dynamics. It is reported in the literature that the micropolar fluid theory [6, 7], an augmented version of the Navier–Stokes equations, may be advantageous for experiments in microchannels. As the characteristic length of a device decreases, the Reynolds number becomes smaller, typically between 1 and 10, with mass transport phenomena led by viscosity rather than inertial forces, as would occur at the macro-scale. At a low Reynolds number, turbulent mixing is neglected and two different fluids can only mix by pure diffusion with a long diffusion time, which can be advantageous in the fabrication of a three-electrode system inside the microchannels [8] and disadvantageous in the case of protein folding, where some optimization algorithms must be developed to minimize the mixing time [9]. An exhaustive review of the physics of microfluidics with special emphasis on biotechnology can be found in [10]. One of the most frequently used applications of MHD flows in the scientific and engineering community is the development of devices where the electromagnetic field is used to drive the flow inside a channel. In contrast to macro-scale mechanical pumps where moving parts as actuators are used to pump the flow, non-mechanical pumps as using electrohydrodynamics (EHD) [11, 12] or electrokinetics [13] are increasingly being used in microfluidics for their simplicity of fabrication and the absence of fatigue problems compared to the traditional micropump. Moreover, both the direct current (DC) [14–16] and the alternate current (AC) [17] MHD micropumps have additional advantages such as lower actuation voltages, continuous and bi-directional fluid flow, and the ability to pump fluids with medium and high electrical conductivity. For example, a common problem for the DC micropump includes the degradation of the electrodes by the Faradaic process, the formation of bubbles due to electrolysis when the aqueous solution is used as a working fluid, and the Joule heating effect. In the AC-MHD micropump, the formation of bubbles does not occur, and the presence of additional eddy currents increases the Joule heating, which limits the intensity of the magnetic field at high frequencies [18]. The working principle for MHD micropumps is given by the Lorentz force

$$\mathbf{F}_L = \mathbf{j} \times \mathbf{B}, \tag{1.1}$$

where $\mathbf{j}$ is the electric current density of the flow and $\mathbf{B}$ is the magnetic flux density. This force is generated by the interaction between the external magnetic field by means of permanent magnets or electromagnets, and the electric current through mutually orthogonal electrodes. When the fluid flow moves with the velocity $\mathbf{v}$, the electrical current density $\mathbf{j}$ can be expressed as

$$\mathbf{j} = \sigma(\mathbf{E} + \mathbf{v} \times \mathbf{B}), \tag{1.2}$$

which means that the Lorentz force (1.1) becomes

$$\mathbf{F}_L = \sigma(\mathbf{E} + \mathbf{v} \times \mathbf{B}) \times \mathbf{B}, \tag{1.3}$$

where σ is the electrical conductivity of the flow. It is important to highlight that most of the numerical investigations of the fluid flow inside an MHD micropump have been carried out only for incompressible flows; however, the real fluid flow in place is compressible. Patel and Kassegne [19] developed a general numerical solver for three-dimensional MHD micropumps with a channel length of 20 mm, electrode length of 16 mm, electrical conductivity of 1.5 S/m and thermal conductivity of 0.6 W/(m · K). They also investigated the effects of electroosmosis and Joule heating in a rectangular and trapezoidal microchannel. Wang et al. [20] investigated two-dimensional fully-developed stationary incompressible MHD flow with the use of the Finite Difference Method (FDM) for a channel of length 44 cm and electrode length of 35 mm in a saline solution (NaCl) with a conductivity of 1.5 S/m and in a liquidous Gallium (Ga) flow with an electrical conductivity of $7.30 \cdot 10^6$ S/m, concluding that the channel dimensions and the induced Lorentz forces have significant influences on the fluid flow velocity. Lim and Choi [21] solved the incompressible MHD equations with an in-house FDM based solver and with the commercial CFD-ACE Finite Volume Method (FVM) for a phosphate-buffered saline (PBS) solution inside a microchannel of length 30 mm with $\sigma = 1.5$ S/m. Hasan et al. [22] performed a comparative study on the performance of the micropump with different cross-sections through the Finite Element Method (FEM) using again the PBS solution as filling fluid. The Lattice Boltzmann Method (LBM) particle-based simulation of a two-dimensional incompressible transient flow and heat transfer phenomena for a DC-MHD micropump with a length of 22 mm was performed by Chatterjee and Amiroudine [23], showing the ability to extend the model for the investigation of a three-dimensional AC-MHD micropump. In the present work, we focus on a transient compressible, viscous fluid flow phenomenon, which can be called a magnetogasdynamic micro-shock wave propagation benchmark problem. Therefore, it is important to note that for both macrochannels and microchannels, the rupture of a membrane separating two states of a gas at different pressure and causes the formation of an unsteady flow composed by a fan of acoustic waves, i.e., shock, rarefaction and compression waves. These acoustic waves are extensively used for medical purposes, e.g., from non-invasive cancer treatment [24] to removal of kidney stones [25].

The physical behavior of shock wave propagation in compressible, viscous flows in macroscale channels has been widely studied both experimentally and numerically, although the knowledge is still not satisfactory on the simulation of micro-shock wave propagations at the microscale [26]. Furthermore, a knowledge gap can be identified in the investigation of compressible, viscous flows in a micro-shock benchmark channel where the electrically conducting gasflow is exposed to an external magnetic field. Therefore, the present work black attempts to contribute to this challenging research field through the numerical investigation of an electrically conducting compressible, viscous fluid flow in the case of a micro-shock channel benchmark problem where the gasflow is exposed to a uniform and stationary external magnetic field. In this work, the Lorentz force (1.1) has been added as a source term to the unsteady, fully compressible Navier–Stokes equations discretized with the nodal Discontinuous Galerkin-Finite Element Method (DG-FEM). For solving the governing equations discussed in Section 2, a DG-FEM based open-source MATLAB code has been used that was developed by Hesthaven and Warburton [27] and further improved for microfluidic gasflow applications by Zingaro and Könözsy [28].

2. Methodology

2.1. **Governing equations and their solution approach.**

The conservative form of the two-dimensional governing equations for compressible, viscous Newtonian fluid flows can be formulated for the density ρ, x-momentum ρu, y-momentum ρv, the total energy E transport equation, and the total pressure p. For two-dimensional compressible flows, the scalar form of the continuity equation can be expressed by

$$\frac{\partial \rho}{\partial t} + \frac{\partial}{\partial x}(\rho u) + \frac{\partial}{\partial y}(\rho v) = 0, \tag{2.1}$$

the Navier–Stokes momentum equations for the velocity components u and v are

$$\frac{\partial}{\partial t}(\rho u) + \frac{\partial}{\partial x}(\rho u^2 + p) + \frac{\partial}{\partial y}(\rho u v) = \frac{\partial \tau_{xx}}{\partial x} + \frac{\partial \tau_{xy}}{\partial y} + \rho F_{L_x}, \tag{2.2}$$

$$\frac{\partial}{\partial t}(\rho v) + \frac{\partial}{\partial x}(\rho u v) + \frac{\partial}{\partial y}(\rho v^2 + p) = \frac{\partial \tau_{yx}}{\partial x} + \frac{\partial \tau_{yy}}{\partial y} + \rho F_{L_y}, \tag{2.3}$$

and the total energy equation transport equation can be written as

$$\frac{\partial E}{\partial t} + \frac{\partial}{\partial x}\left[(E+p)u\right] + \frac{\partial}{\partial y}\left[(E+p)v\right] = \frac{\partial}{\partial x}(\tau_{xx}u + \tau_{xy}v) + \frac{\partial}{\partial y}(\tau_{yx}u + \tau_{yy}v) +$$

$$+ \frac{\partial}{\partial x}\left(k\frac{\partial T}{\partial x}\right) + \frac{\partial}{\partial y}\left(k\frac{\partial T}{\partial y}\right) + \rho\left(F_{L_x}u + F_{L_y}v\right), \tag{2.4}$$

where k is the thermal conductivity coefficient. For compressible fluid flows, the viscous stress tensor based on the Navier–Stokes hypothesis is

$$\underline{\underline{\tau}} = 2\mu \underline{\underline{S}} - \frac{2}{3}\mu\left(\nabla \cdot \mathbf{v}\right)\underline{\underline{I}}, \tag{2.5}$$

where μ is the temperature dependent dynamic viscosity which can be computed by using the Sutherland law, see details in [28]. The rate-of-strain tensor $\underline{\underline{S}}$ in equation (2.5) can be expressed with vector notation as

$$\underline{\underline{S}} = \frac{1}{2}\left[(\nabla \otimes \mathbf{v}) + (\nabla \otimes \mathbf{v})^T\right], \tag{2.6}$$

where $\underline{\underline{I}}$ is the unit tensor. The elements of the viscous stress tensor (2.5) for two-dimensional compressible, viscous fluid flows are

$$\tau_{xx} = 2\mu\frac{\partial u}{\partial x} - \frac{2}{3}\mu\left(\frac{\partial u}{\partial x} + \frac{\partial v}{\partial y}\right), \tag{2.7}$$

$$\tau_{xy} = \tau_{yx} = \mu\left(\frac{\partial u}{\partial y} + \frac{\partial v}{\partial x}\right), \tag{2.8}$$

$$\tau_{yy} = 2\mu\frac{\partial v}{\partial y} - \frac{2}{3}\mu\left(\frac{\partial u}{\partial x} + \frac{\partial v}{\partial y}\right). \tag{2.9}$$

The total energy E can be expressed through the equation of state for ideal gases as

$$E = \frac{p}{\gamma - 1} + \frac{\rho}{2}(u^2 + v^2), \tag{2.10}$$

where γ is the specific heat capacity assumed here to be equal to 1.66 following the work of Zeitoun et al. [26] for a monoatomic gas. Based on the assumption that MHD flows are defined as electrically conducting fluids under the application of an external magnetic field, the external electrical field $\mathbf{E}$ is neglected in equation (1.2), thus the electrical current density is $\mathbf{j} = \sigma(\mathbf{v} \times \mathbf{B})$ in the present model. Therefore, the two-dimensional Lorentz force can be expressed as

$$\begin{cases} F_{L_x} = \sigma(-uB_y^2 + vB_xB_y), \\ F_{L_y} = \sigma(uB_xB_y - vB_x^2). \end{cases} \tag{2.11}$$

The set of governing equations (2.1)–(2.11) can be written in a compact form as

$$\frac{\partial \mathbf{u}}{\partial t} + \frac{\partial}{\partial x}(\mathbf{f}_c - \mathbf{f}_v) + \frac{\partial}{\partial y}(\mathbf{g}_c - \mathbf{g}_v) = \mathbf{s}, \tag{2.12}$$

where $\mathbf{u} = \mathbf{u}(\mathbf{x}, t) = [\rho, \rho u, \rho v, E]^T$ is the vector of the conservative variables, and

$$\mathbf{f}_c = \left[\rho u, \rho u^2 + p, \rho uv, (E + p)u\right]^T \quad \text{and} \quad \mathbf{f}_v = [0, \tau_{xx}, \tau_{yx}, \tau_{xx}u + \tau_{xy}v]^T$$

are the convective and viscous fluxes along the x and y directions, while

$$\mathbf{g}_c = \left[\rho v, \rho uv, \rho v^2 + p, (E + p)v\right]^T \quad \text{and} \quad \mathbf{g}_v = [0, \tau_{xy}, \tau_{yy}, \tau_{xy}u + \tau_{yy}v]^T,$$

and the vector $\mathbf{s} = \left[0, \rho F_{L_x}, \rho F_{L_y}, \rho(F_{L_x}u + F_{L_y}v)\right]^T$ expresses the source term. By incorporating the fluxes in a single matrix operator $\mathbf{f}$, the governing equations in the domain Ω are given by a system of coupled nonlinear mixed hyperbolic-parabolic partial differential equations (PDEs) as follows:

$$\frac{\partial \mathbf{u}}{\partial t} + \nabla \cdot \mathbf{f} = \mathbf{s}, \tag{2.13}$$

with an additional initial condition at time t_0 and boundary conditions on the boundary $\partial\Omega$. The numerical approximation of the problem above can be formulated as

$$\frac{\partial \mathbf{u}_h}{\partial t} + \nabla \cdot \mathbf{f}_h = \mathbf{s}_h, \tag{2.14}$$

where the numerical solution $\mathbf{u}_h$ and the spatial operator $\nabla \cdot \mathbf{f}_h$ have been discretized with the nodal DG-FEM scheme [27] and then temporally integrated with the fourth-order Runge–Kutta scheme [28]. Note that the verification of the implementation of the governing equations (2.1)–(2.4) was carried out by Zingaro and Könözsy [28] for another multiphysics problem in the framework of the nodal DG-FEM approach. However, the implementation of the magnetic force terms (2.11) with an investigation of the variation of the electrical conductivity σ for a magnetogasdynamic microflow at different magnetic Reynolds numbers is carried out in this work.

2.2. **Spatial discretization.** The physical domain of the microchannel $\Omega \in \mathbb{R}^2$ is replaced by the computational domain Ω_h composed by the union of K non-overlapping triangular elements D_k, with $k = 1 \dots K$. In each element, the local solution $\mathbf{u}_h^k(\mathbf{x}, t)$, belonging in the space

$$\mathbf{V}_h = \{\mathbf{v}_h \in (L^2(\Omega_h))^d : \mathbf{u}_{h|D_k} \in (\mathcal{P}_N)^d, \forall D_k \in D_h\}, \quad d = 2, \tag{2.15}$$

is approximated by

$$x \in D_k : \mathbf{u}_h^k(\mathbf{x}, t) = \sum_{i=1}^{N_p} \mathbf{u}_h^k(\mathbf{x}, t) l_i^k(\mathbf{x}), \tag{2.16}$$

where the N-th order piece-wise polynomial expansion of the local multidimensional Lagrange polynomial $l_i^k(\mathbf{x})$ is based on the grid points x_i with $N_p = \frac{(N+1)(N+2)}{2}$ unknown coefficient u_h^k. The global solution of the nonlinear system is recovered by the direct sum of K local polynomials $\mathbf{u}_h^k(\mathbf{x}, t)$ as follows:

$$\mathbf{u}(\mathbf{x}, t) \simeq \mathbf{u}_h(\mathbf{x}, t) = \bigoplus_{k=1}^{K} \mathbf{u}_h^k(\mathbf{x}, t). \tag{2.17}$$

To achieve accurate results with the numerical integration and differentiation, each triangle $\mathbf{x} \in D_k$ is mapped to a reference triangle $\mathbf{r} \in I_k \in [1, -1]$ through a linear mapping, thus the new local solution can be expressed by

$$x \in I_k : \mathbf{u}_h^k(\mathbf{r}, t) = \sum_{i=1}^{N_p} \mathbf{u}_h^k(\mathbf{r}_i, t) l_i^k(\mathbf{r}), \tag{2.18}$$

where the two-dimensional Legendre–Gauss–Lobatto grid points $\mathbf{r}_i$ are chosen to improve the quality of the local interpolating polynomial solution.

In the DG-FEM formulation, the governing equations (2.13) are satisfied elementwise through the L^2 orthogonality between the residual $\frac{\partial \mathbf{u}_h}{\partial t} + \nabla \cdot \mathbf{f}_h - \mathbf{s}_h$ and all the test functions $\phi_h(\mathbf{x}) \in \mathbf{V}_h$ which belong to the same functional space of the multidimensional Lagrange interpolating polynomial $l_i^k(\mathbf{x})$, thus

$$\int_{D_k} \left[\left(\frac{\partial \mathbf{u}_h^k}{\partial t} + \nabla \cdot \mathbf{f}_h - \mathbf{s}_h \right) \phi_h(\mathbf{x}) \right] d\mathbf{x} = \mathbf{0}. \tag{2.19}$$

By applying the Gauss theorem, the weak formulation of the DG-FEM is obtained as

$$\int_{D_k} \left[\frac{\partial \mathbf{u}_h^k}{\partial t} l_i^k(\mathbf{x}) - \mathbf{f}_h^k \cdot \nabla l_i^k(\mathbf{x}) - \mathbf{s}_h l_i^k(\mathbf{x}) \right] d\mathbf{x} = - \oint_{\partial D_k} \mathbf{f}^* \; l_i^k(\mathbf{x}) \cdot \hat{\mathbf{n}} d\mathbf{x}. \tag{2.20}$$

The choice of the numerical flux $\mathbf{f}^*$ term is essential for the accurate modeling of the physical problem, which ensures the stability of the scheme and the uniqueness of the solution at the interface of two adjacent elements. In this work, the local Lax-Friedrichs flux scheme [29] has been chosen for its simplicity. To avoid stability problems due to the spurious unphysical oscillations resulting from the large gradient flows, the slope limiter proposed by Tu and Aliabadi [30] has been employed black in this work. Note that for more accurate MHD flow simulations, i.e., to improve the accuracy of the solution, the Harten–Lax–van Leer Discontinuities (HLLD) approximate Riemann solver [31] can be implemented, which should be the subject of future work.

2.3. **Temporal discretization.** The Initial Value Problem (IVP) of the system of ordinary differential equations (ODEs) resulting from the spatial DG-FEM discretization $\mathcal{L}(\mathbf{u}_h, t)$ at time t_0 is

$$\begin{cases} \frac{d\mathbf{u}_h}{dt} = \mathcal{L}(\mathbf{u}_h, t), \\ \mathbf{u}_h(t_0) = \mathbf{u}_h^0, \end{cases} \tag{2.21}$$

which has been solved with a fourth-order Low Storage Explicit Runge–Kutta (LSERK) scheme from [32] as follows:

$$\begin{cases} \mathbf{p}^{(0)} = \mathbf{u}_h^n, \\ \text{for i } \in [1, ..., 5] : \begin{cases} \mathbf{k}^i = a_i \mathbf{k}^{(i-1)} + \Delta t \mathcal{L}_h(\mathbf{p}^{(i-1)}, t_n + c_i \Delta t), \\ \mathbf{p}^{(i)} = \mathbf{p}^{(i-1)} + b_i \mathbf{k}^i, \end{cases} \\ \mathbf{u}_h^{n+1} = \mathbf{p}^{(5)}. \end{cases} \tag{2.22}$$

The time integration scheme (2.22) guarantees the numerical stability for non-linear problems and is suitable for problems with shock waves and discontinuities. The coefficients in equation (2.22) and the equation for the time step can be found in [28].

2.4. **Source term discretization.** In the present numerical study, a uniform and a stationary external magnetic field is applied in the y spatial direction and it varies in its strength as a function of the x spatial coordinate, which is defined as

$$\mathbf{B} = (0, B_y(x), 0). \tag{2.23}$$

In the presence of homogenous media, the magnetic flux density $B_y(x)$ can be expressed as a linear function of the magnetic intensity $H_y(x)$ as

$$B_y(x) = \mu_0 H_y(x), \tag{2.24}$$

where μ_0 is the permeability of the medium. The mathematical expression for $H_y(x)$ has been taken from the work of Tzirtzilakis and Loukopoulos [33] as follows:

$$H_y(x) = \frac{H_0}{2}\left[\tanh(a_1(x - x_1)) - \tanh(a_2(x - x_2))\right], \tag{2.25}$$

where H_0 defines the magnitude of the magnetic intensity and the constants a_1 and a_2 specify the magnetic field gradient at the points x_1 and x_2, respectively.

2.5. **The benchmark test problem.** The viscous micro-shock channel benchmark problem proposed by Zeitoun et al. [26] has been adapted here in which case the variation of the electrical conductivity σ was neglected at different magnetic Reynolds numbers. Therefore, the viscous micro-shock channel test problem of Zeitoun et al. [26] can be considered as a reference test case for our study, because our aim is to investigate the effect of the variation of the electrical conductivity σ on a magnetogasdynamic microflow at different magnetic Reynolds numbers. The schematic of the viscous micro-shock channel benchmark problem is shown in Figure 1.

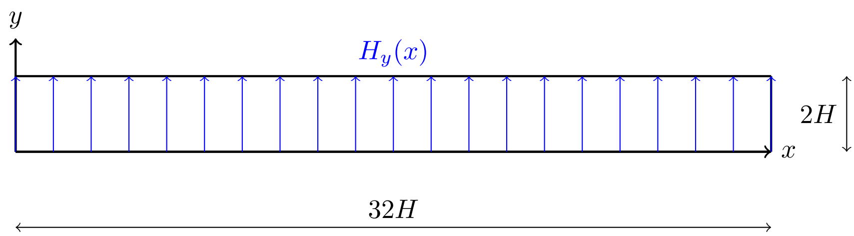

Figure 1. The geometry of the microchannel with the hydraulic diameter of $H = 2.55$ mm to investigate a magnetogasdynamic flow

At the initial time $t_0 = 0$ s, the gas is separated by one membrane positioned at $x_d = 29.69$ mm into two states, whose values for pressure and density are shown in Table 1 following the previous work of Zingaro and Könözsy [28].

ρ_L [kg/m^3]	$8.43 \cdot 10^{-3}$
ρ_R [kg/m^3]	$7.08 \cdot 10^{-4}$
p_L [Pa]	525.98
p_R [Pa]	44.2

Table 1. Numerical values of pressure and density at the left (p_L, ρ_L) and right (p_R, ρ_R) section of the viscous micro-shock channel [28]

The initial conditions before and after the rupture of the membrane, taken from the previous work of Zeitoun et al. [26], are

$$\rho(x,y,0) = \begin{cases} \rho_L & x < x_d, \qquad (x_d = 29.69\,\text{mm}), \\ \rho_R & x \geq x_d, \end{cases} \tag{2.26}$$

$$u(x,y,0) = 0, \tag{2.27}$$

$$v(x,y,0) = 0, \tag{2.28}$$

$$p(x,y,0) = \begin{cases} p_L & x < x_d, \qquad (x_d = 29.69\,\text{mm}), \\ p_R & x \geq x_d, \end{cases} \tag{2.29}$$

and the boundary conditions are no-slip at the left and right walls of the microchannel. For this benchmark test problem, a grid convergence/mesh sensitivity study has already been carried out on different mesh sizes in the previous work of Zingaro and Könözsy [28] for the numerical solution of the compressible, viscous Navier–Stokes equations without the inclusion of the electromagnetic field (see Table 2). Therefore, the fine mesh employed by Zingaro and Könözsy [28] has also been adopted here, because an accurate numerical solution for the benchmark test problem of Zeitoun et al. [26] can be obtained [28]. The details of different grid size resolutions are shown in Table 2, where N_x and N_y are the number of grid points in x and y coordinates, and Δx and Δy are the grid spacing in x and y directions, respectively.

Mesh	N_x	N_y	Δx [mm]	Δy [mm]
Coarse	97	7	$8.33 \cdot 10^{-1}$	$8.33 \cdot 10^{-1}$
Medium	193	13	$4.17 \cdot 10^{-1}$	$4.17 \cdot 10^{-1}$
Fine	385	25	$2.08 \cdot 10^{-1}$	$2.08 \cdot 10^{-1}$

Table 2. Grid resolutions used in this study and in the previous work [28]

The simulations presented here have been performed with a first-order polynomial approximation for the spatial terms to ensure the monotonicity behavior of the discretization scheme with a fourth-order Low Storage Explicit Runge–Kutta (LSERK) scheme for the temporal part.

3. Results and Discussion

The investigation of the impact of the electromagnetic field on the viscous micro-shock channel is carried out through a variation of the flow conductivity σ which affects the magnetic Reynolds number defined as $Re_m = \sigma\mu_0\bar{v}\ell$, where $\mu_0 = 1.4 \cdot 10^{-6}$ H/m is the magnetic permeability, $\bar{v} = 0.4$ m/s is the mean velocity along the height of the microchannel, and $\ell = 2.5 \cdot 10^{-3}$ m is the characteristic length. The magnetic Reynolds number is defined as the ratio between the advective and diffusive forces of the magnetic field and in this work different low Re_m are computed through a variation of the electrical conductivity σ (see Table 3) in such a way that the low magnetic Reynolds number assumption [34], commonly used in microfluidics, holds. Furthermore, for the sake of simplicity, the thermal conductivity coefficient k is considered to be constant in the total energy equation (2.4) with the value of 0.0172 W/(mK).

Electrical conductivity σ [S/m]	**Magnetic Reynolds numbers** [–]
100	$1.4 \cdot 10^{-7}$
$1.0 \cdot 10^{3}$	$1.4 \cdot 10^{-6}$
$5.0 \cdot 10^{3}$	$7.0 \cdot 10^{-6}$
$10 \cdot 10^{3}$	$14 \cdot 10^{-6}$

Table 3. Magnetic Reynolds numbers Re_m computed based on different electrical conductivity coefficient σ

The low magnetic Reynolds number assumption [34] implies that at the current length, even in the presence of high electrical conductivity σ, the magnetic field exhibits a dissipative behavior that spreads out rather than being advected by the flow. To gain a better insight into the physical behavior of the acoustic waves generated behind and in front of the rupture of the membrane, the profiles of the relevant quantities are non-dimensionalized with their respective values of the driven section and extracted at the centerline ($y = H$) of the microchannel (see Figure 2). Furthermore, the physical time scale of the investigated experimental micro-shock channel benchmark problem of Zeitoun et al. [26] is extremely short, i.e., 80 μ; therefore, the analysis of the complex flow physics originating from the reflection of the acoustic waves against the lateral wall has not been addressed in the present work and it is recommended as a future topic of research.

It has been found that there are no visible effects of the electrical conductivity investigated for $\sigma = 100\,\mathrm{S/m}$; visible effects start from $\sigma = 1 \cdot 10^{3}\,\mathrm{S/m}$. As the electrical conductivity σ is further increased, all the variables change the characteristic behavior of their profiles substantially. Regarding the pressure (see Figure 2a), for $\sigma = 10 \cdot 10^{3}\,\mathrm{S/m}$, a strong and fast shock wave moves to the right, followed by a smooth expansion fan, while the contact discontinuity is no longer visible. Similar to the pressure, velocity and temperature profiles are subject to a rapid increase in the shock wave region, where again the flow is moves to the right of the microchannel (see Figures 2b and 2c). The increase in the temperature might be explained through the Joule heating effect, while the increase in the velocity can be explained based on the effect of the Lorentz force, which is able to accelerate the flow in the x spatial direction. The density profile is characterized by the presence of a constant state in the center of the shock tube with a consequent change in the position and the magnitude of the shock wave (see Figure 2d). Furthermore, a comparison can be plotted with the reference values taken from the work of Zeitoun et al. [26] for the temperature and density profiles in Figures 2c and 2d, respectively.

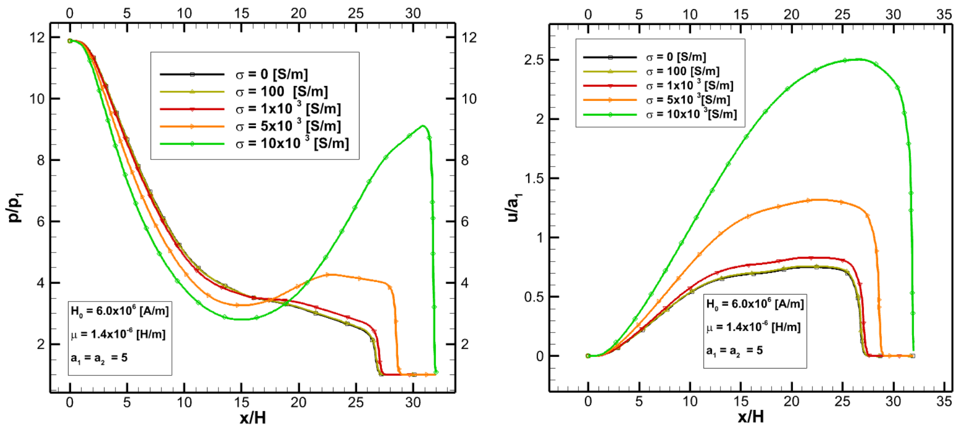

(a) Pressure profile (b) Velocity profile

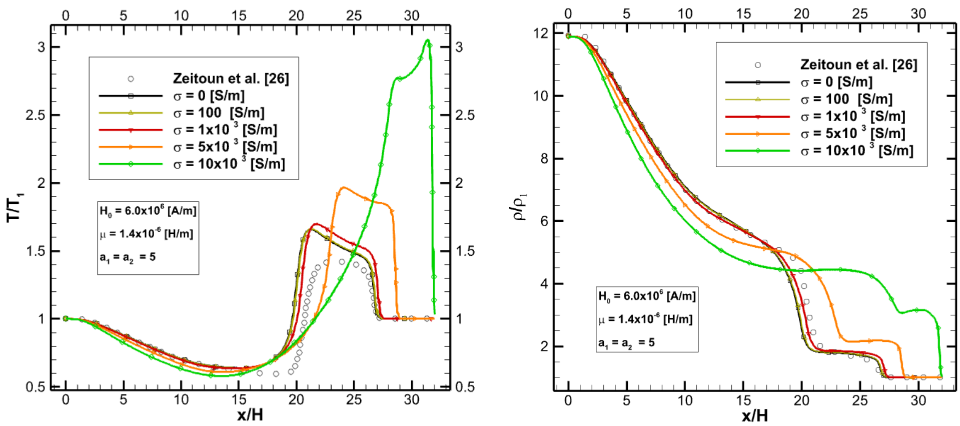

(c) Temperature profile (d) Density profile

Figure 2. Effects of the electrical conductivity σ on different flow field variables extracted at the centerline of the microchannel

The magnetic field gradient in the points x_1 and x_2 is controlled by the two constants a_1 and a_2 in equation (2.25), which has been taken from the work of Tzirtzilakis and Loukopoulos [33] to simulate a physically realistic phenomenon relevant to biomedical applications. Figure 3 shows the effect of three different values for a_1 and a_2 on the dimensionless magnetic intensity H/H_0 for $\sigma = 5 \cdot 10^3\,\mathrm{S/m}$ and $H_0 = 6.0 \cdot 10^6\,\mathrm{A/m}$, respectively. The numerical results suggest that the magnetic field intensity is slightly affected by changes in the magnitude of the magnetic field gradient. For $a_1 = a_2 = 10$, the magnetic field intensity has a semi-quadratic variation over the entire microchannel, while it remains constant for $a_1 = a_2 = 1$ and $a_1 = a_2 = 2$.

In Figures 4, 5, 6 and 7, the contour plots of the temperature, pressure, density and the velocity component u at $\sigma = 5 \cdot 10^3\,\mathrm{S/m}$ are shown in comparison with the value of the electrical conductivity $\sigma = 0\,\mathrm{S/m}$ as a reference value. The numerical solution is obtained by solving the compressible, viscous Navier-Stokes equations (2.1)–(2.4) with the inclusion of the Lorentz force terms (2.11) as source terms using the DG-FEM discretization approach discussed in Section 2. It has been observed regarding all the conservative variables that the left portion of the microchannel is not influenced by the magnetic field, whereas in the right section, the effect of the Lorentz force is particularly visible.

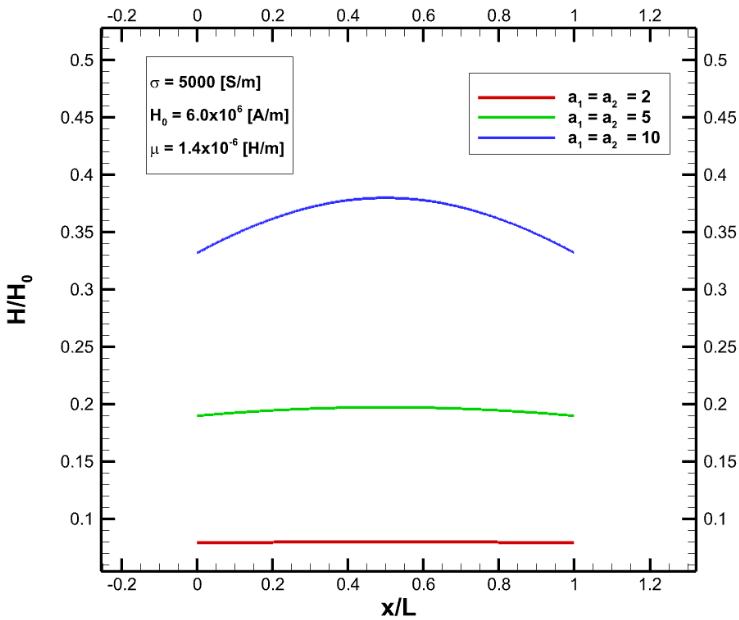

Figure 3. Magnetic field intensity for three different a_1, a_2 values

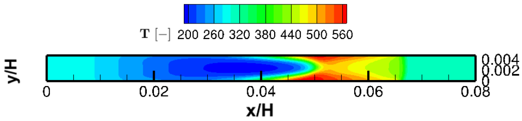

(a) Solution of the compressible Navier–Stokes equations without the Lorentz force terms

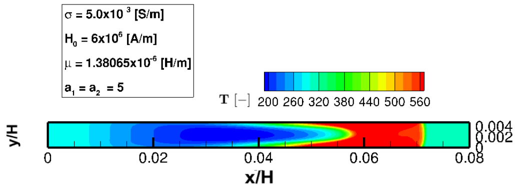

(b) Solution of the compressible Navier–Stokes equations with the MHD Lorentz force terms

Figure 4. Temperature distribution in the microchannel

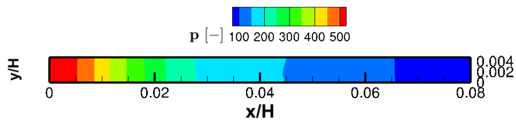

(a) Solution of the compressible Navier–Stokes equations without the Lorentz force terms

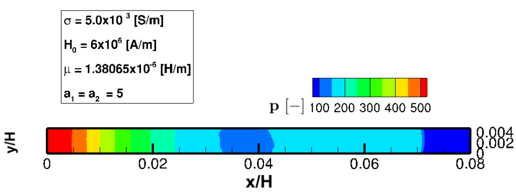

(b) Solution of the compressible Navier–Stokes equations with the MHD Lorentz force terms

Figure 5. Pressure distribution in the microchannel

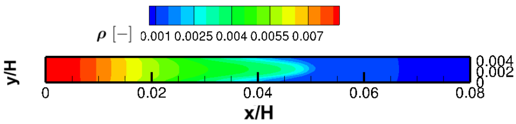

(a) Solution of the compressible Navier–Stokes equations without the Lorentz force terms

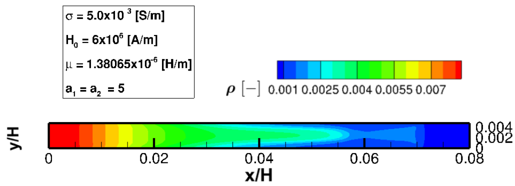

(b) Solution of the compressible Navier–Stokes equations with the MHD Lorentz force terms

Figure 6. Density distribution in the microchannel

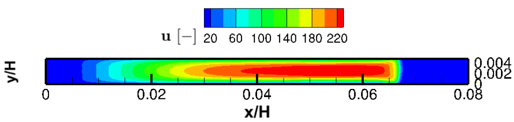

(a) Solution of the compressible Navier–Stokes equations without the Lorentz force terms

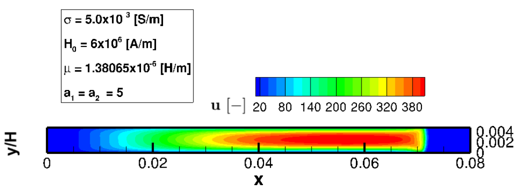

(b) Solution of the compressible Navier–Stokes equations with the MHD Lorentz force terms

Figure 7. Velocity component u distribution in the microchannel

4. Conclusions and Future Work

In this work, the effect of the electrical conductivity coefficient σ on a two-dimensional compressible, viscous micro-shock channel was analyzed behind the rupture of a membrane which separates two states of the same gas initially at rest. The Lorentz force terms (2.11) were included as source terms in the compressible Navier–Stokes equations (2.3), which were discretized with the use of the Discontinuous Galerkin-Finite Element Method (DG-FEM). Different magnetic Reynolds numbers were considered along with the variation of the electrical conductivity σ of the flow, from $\sigma = 100\,\mathrm{S/m}$ to $\sigma = 10 \cdot 10^3\,\mathrm{S/m}$. The acoustic waves after $80\mu s$ behind the rupture rupture point of the membrane were investigated. The numerical results suggest that the Lorentz force has a significant impact on the flow field variables from $\sigma > 100\,\mathrm{S/m}$. As the electrical conductivity σ is increased, all the conservative variables (temperature, pressure, density and velocity) showed a significant increase in their quantity toward the right section of the magnetogasdynamic microchannel. In particular, the temperature jump may be caused by the Joule effect while the sharp increase in the velocity profile can be explained by the acceleration of the flow produced by the Lorentz force terms (2.11) in the compressible Navier–Stokes equations (2.3). To achieve high-order spatial accuracy of the numerical solution and obtain even a more accurate prediction of the acoustic waves, the implementation of the Harten–Lax–van Leer Discontinuities (HLLD) Riemann solver [31] is recommended as future work. Furthermore, it is suggested to increase the physical time of the numerical simulation to get insights on the complex flow physics originating from the reflection of the acoustic waves against the lateral wall and to verify the stability of the present numerical scheme.

Acknowledgement. This project was financially supported by the Centre for Computational Engineering Sciences at Cranfield University under project code EEB6001R. For the purpose of open access, the authors have applied a Creative Commons Attribution (CC BY) licence to any author-accepted manuscript version arising.

References

1. Lawal, M. O. and Ajadi, S. O. "The behavior of MHD flow and heat transfer in the presence of heat source and chemical reaction over a flat plate." *Journal of Computational and Applied Mechanics,* **11**(2), (2016), pp. 159–178.
2. Sekhar, T. V. S., Sivakumar, R., and Kumar, H. "Numerical solutions for steady viscous flow past a circular cylinder in an aligned magnetic field." *Journal of Computational and Applied Mechanics,* **9**(2), (2014), pp. 201–217.
3. Stott, S. L., Hsu, Chia-Hsien, Tsukrov, D. I., Yu, Min, Miyamoto, D. T., Waltman, B. A, Rothenberg, S. M., Shah, A. M., Smas, M. E., Korir, G. K., et al. "Isolation of circulating tumor cells using a microvortex-generating herringbone-chip." *Proceedings of the National Academy of Sciences,* **107**(43), (2010), pp. 18392–18397. doi: 10.1073/pnas.1012539107.
4. Zhao, Y., Chen, D., Yue, H., French, J. B., Rufo, J., Benkovic, S. J., and Huang, T. J. "Lab-on-a-chip technologies for single-molecule studies". *Lab on a Chip,* **13**(12), (2013), pp. 2183–2198. doi: 10.1039/c3lc90042h.

5. Shaw, S. "Mathematical model on magnetic drug targeting in microvessel." *Magnetism and Magnetic Materials.* Ed. by Neeraj Panwar. IntechOpen, 2018, pp. 83–107. doi: 10.5772/intechopen.68579.
6. Hegab, H. E. and Liu, G. "Fluid flow modeling of micro-orifices using micropolar fluid theory." *Microfluidic Devices and Systems III.* Vol. 4177. Society of Photo-Optical Instrumentation Engineers. 2000, pp. 257–267. doi: 10.1117/12.395670.
7. Aissa, W. A. and Mohammadein, A. A. "Joule heating effects on a micropolar fluid past a stretching sheet with variable electric conductivity." *Journal of Computational and Applied Mechanics* **6**(1), (2005), pp. 3–13.
8. Kenis, P. J., Ismagilov, R. F., and Whitesides, G. M. "Microfabrication inside capillaries using multiphase laminar flow patterning". *Science,* **285**(5424), (1999), pp. 83–85. doi: 10.1126/science.285.5424.83.
9. Hertzog, D. E., Ivorra, B., Mohammadi, B., Bakajin, O., and Santiago, J. G. "Optimization of a microfluidic mixer for studying protein folding kinetics". *Analytical Chemistry,* **78**(13), (2006), pp. 4299–4306. doi: 10.1021/ac051903j.
10. Squires, T. M. and Quake, S. R. "Microfluidics: Fluid physics at the nanoliter scale." *Reviews of Modern Physics,* **77**(3), (2005), pp. 977–1026. doi: 10.1103/RevModPhys.77.977.
11. Bart, S. F., Tavrow, L. S., Mehregany, M., and Lang, J. H. "Microfabricated electrohydrodynamic pumps." *Sensors and Actuators A: Physical,* **21**(1-3) (1990), pp. 193–197. doi: 10.1016/0924-4247(90)85037-5.
12. Richter, A., Plettner, A., Hofmann, K. A., and Sandmaier, H. "A micromachined electrohydrodynamic (EHD) pump." *Sensors and Actuators A: Physical,* **29**(2), (1991), pp. 159–168. doi: 10.1016/0924-4247(91)87118-M.
13. Manz, A., Effenhauser, C. S., Burggraf, N., Harrison, D. J., Seiler, K., and Fluri, K. "Electroosmotic pumping and electrophoretic separations for miniaturized chemical analysis systems." *Journal of Micromechanics and Microengineering,* **4**(4), (1994), p. 257. doi: 10.1088/0960-1317/4/4/010.
14. Jang, J. and Lee, S. S. "Theoretical and experimental study of MHD (magnetohydrodynamic) micropump." *Sensors and Actuators A: Physical,* **80**(1), (2000), pp. 84–89. doi: 10.1016/S0924-4247(99)00302-7.
15. Nguyen, B. and Kassegne, S. K. "High-current density DC magenetohydrodynamics micropump with bubble isolation and release system." *Microfluidics and Nanofluidics,* **5**(3), (2008), pp. 383–393. doi: 10.1007/s10404-007-0255-3.
16. Homsy, A., Koster, S., Eijkel, J. C. T., Berg, A., Lucklum, F., Verpoorte, E., and Rooij, N. F. "A high current density DC magnetohydrodynamic (MHD) micropump." *Lab on a Chip,* **5**(4), (2005), pp. 466–471.
17. Lemoff, A. V. and Lee, A. P. "An AC magnetohydrodynamic micropump." *Sensors and Actuators B: Chemical,* **63**(3), (2000), pp. 178–185. doi: 10.1016/S0925-4005(00)00355-5.

18. Eijkel, J. C. T., Dalton, C., Hayden, C. J., Burt, J. P. H., and Manz, A. "A circular ac magnetohydrodynamic micropump for chromatographic applications." *Sensors and Actuators B: Chemical,* **92**(1-2), (2003), pp. 215–221. DOI: 10.1016/S0925-4005(03)00267-3.
19. V. Patel and S. K. Kassegne. "Electroosmosis and thermal effects in magnetohydrodynamic (MHD) micropumps using 3D MHD equations." *Sensors and Actuators B: Chemical,* **122**(1), (2007), pp. 42–52. DOI: doi.org/10.1016/j.snb.2006.05.015.
20. Wang, Pei-Jen, Chang, Chia-Yuan, and Chang, Ming-Lang. "Simulation of two-dimensional fully developed laminar flow for a magneto-hydrodynamic (MHD) pump." *Biosensors and bioelectronics,* **20**(1), (2004), pp. 115–121. DOI: 10.1016/j.bios.2003.10.018.
21. Lim, S. and Choi, B. "A study on the MHD (magnetohydrodynamic) micropump with side-walled electrodes." *Journal of Mechanical Science and Technology,* 23(3), (2009), pp. 739–749. DOI: 10.1007/s12206-008-1107-0.
22. Hasan, M. I., Ali, A. J. F., and Tufah, R. S. "Numerical study of the effect of channel geometry on the performance of magnetohydrodynamic micro pump." *Engineering Science and Technology, an International Journal,* **20**(3), (2017), pp. 982–989. DOI: 10.1016/j.jestch.2017.01.008.
23. Chatterjee, D. and Amiroudine, S. "Lattice Boltzmann simulation of thermofluidic transport phenomena in a DC magnetohydrodynamic (MHD) micropump." *Biomedical Microdevices,* **13**(1), (2011), pp. 147–157. DOI: 10.1007/s10544-010-9480-8.
24. Gamarra, F., Spelsberg, F., Dellian, M., and Goetz, A. E. "Complete local tumor remission after therapy with extra-corporeally applied high-energy shock waves (HESW)." *International Journal of Cancer,* **55**(1), (1993), pp. 153–156. DOI: 10.1002/ijc.2910550127.
25. James A. McAteer and Andrew P. E. "The acute and long-term adverse effects of shock wave lithotripsy." *Seminars in Nephrology,* **28**(2), (2008), pp. 200–213. DOI: 10.1016/j.semnephrol.2008.01.003.
26. Zeitoun, D. E., Burtschell, Y., Graur, I. A., Ivanov, M. S., Kudryavtsev, A. N., and Bondar, Y. A. "Numerical simulation of shock wave propagation in microchannels using continuum and kinetic approaches." *Shock Waves,* **19**(4), (2009), pp. 307–316. DOI: 10.1007/s00193-009-0202-1.
27. Hesthaven, J. S. and Warburton, T. *Nodal Discontinuous Galerkin Methods: Algorithms, Analysis, and Applications.* Springer Science & Business Media, 2007.
28. Zingaro, A. and Könözsy, L. "Discontinuous Galerkin finite element investigation on the fully-compressible Navier–Stokes equations for microscale shock-channels." *Aerospace,* **5**(1), (2018), pp. 23–42. DOI: 10.3390/aerospace5010016.
29. Lax, P. D. "Weak solutions of nonlinear hyperbolic equations and their numerical computation." *Communications on pure and Applied Mathematics,* **7**(1), (1954), pp. 159–193. DOI: 10.1002/cpa.3160070112.

30. Tu, S., Aliabadi, S., et al. "A slope limiting procedure in discontinuous Galerkin finite element method for gasdynamics applications." *International Journal of Numerical Analysis and Modeling,* **2**(2), (2005), pp. 163–178.
31. Guo, Xiaocheng, Florinski, V., and Wang, Chi. "The HLLD Riemann solver based on magnetic field decomposition method for the numerical simulation of magneto-hydrodynamics." *Journal of Computational Physics,* **327**, (2016), pp. 543–552. doi: 10.1016/j.jcp.2016.09.057.
32. Carpenter, M. H. and Kennedy, C. A. *Fourth-Order 2N-Storage Runge-Kutta Schemes.* Technical Memorandum NASA-TM-109112. NASA, 1994.
33. Tzirtzilakis, E. E. and Loukopoulos, V. C. "Biofluid flow in a channel under the action of a uniform localized magnetic field." *Computational Mechanics,* **36**(5), (2005), pp. 360–374. doi: 10.1007/s00466-005-0659-4.
34. Cai, Chunpei and Liu, D. D. "Asymptotic solutions for low-magnetic-Reynolds-number gas flows inside a two-dimensional channel." *AIAA journal,* **47**(3), (2009), pp. 542–551. doi: 10.2514/1.37060.